Pore-scale Bubble Population Dynamics of CO2-Foam at Reservoir Pressure

Benyamine Benali[1], Tore Lyngås Føyen[2], Zachary Alcorn[1], Malin Haugen[1], Jarand Gauteplass[1], Anthony R Kovscek[3], and Martin Anders Fernø[1]

[1]University of Bergen
[2]Sintef
[3]Stanford University

November 24, 2022

Abstract

The flow of CO2 foam for mobility control in porous media is dictated by the foam texture, or bubble density, which is commonly expressed as the number of bubbles per unit of flowing gas. In most high-pressure laboratory studies of foam in porous media, the local foam texture cannot be determined due to opaque flow systems. Here, we unlock real-time foam texture dynamics at high pressure (100 bar) by utilizing a realistic pore network with an extended field of view. We identified snap-off as the dominant foam generation mechanism, with additional fining of foam texture caused by backward foam propagation. Foam coalescence during continuous CO2 injection resulted in large gas channels parallel to the general flow direction that reduced the overall foam apparent viscosity. A large fraction of the CO2 foam remained trapped (X_t > 0.97) and stationary in pores to divert CO2 flow and increase sweep efficiency. The gas mobility was calculated from the fraction of trapped bubbles at the pore-scale, and the apparent foam viscosity was in agreement with similar injection test performed at core-scale. Hence, improved understanding of CO2 foam texture evolution (n_f) can strengthen the validation of numerical foam models for physical upscaling of flow phenomena, instrumental in the development of field scale implementation of CO2 foam for in carbon utilization and storage applications.

Pore-scale Bubble Population Dynamics of CO_2-Foam at Reservoir Pressure

Benyamine Benali[1], Tore L. Føyen[1,2,*], Zachary Paul Alcorn[1], Malin Haugen[1], Jarand Gauteplass[1], Anthony R. Kovscek[3] and Martin A. Fernø[1]

[1] Department of Physics and Technology, University of Bergen, Norway

[2] SINTEF Industry, Norway

[3] Department of Energy Resources Engineering, Stanford University, USA

Benyamine Benali (benyamine.benali@uib.no)

Key Points:

- Pore-scale CO_2 foam bubble flow, texture and trapping dynamics at high pressure.
- A comprehensive laboratory investigation of essential foam features and phenomena during dynamic flow supported by the population balance foam model framework.

Abstract

The flow of CO_2 foam for mobility control in porous media is dictated by the foam texture, or bubble density, which is commonly expressed as the number of bubbles per unit of flowing gas. In most high-pressure laboratory studies of foam in porous media, the local foam texture cannot be determined due to opaque flow systems. Here, we unlock real-time foam texture dynamics at high pressure (100 bar) by utilizing a realistic pore network with an extended field of view. We identified snap-off as the dominant foam generation mechanism, with additional fining of foam texture caused by backward foam propagation. Foam coalescence during continuous CO_2 injection resulted in large gas channels parallel to the general flow direction that reduced the overall foam apparent viscosity. A large fraction of the CO_2 foam remained trapped ($X_t > 0.97$) and stationary in pores to divert CO_2 flow and increase sweep efficiency. The gas mobility was calculated from the fraction of trapped bubbles at the pore-scale, and the apparent foam viscosity was in agreement with similar injection test performed at core-scale. Hence, improved understanding of CO_2 foam texture evolution (n_f) can strengthen the validation of numerical foam models for physical upscaling of flow phenomena, instrumental in the development of field scale implementation of CO_2 foam for in carbon utilization and storage applications.

1 Introduction

Foam is a promising method for reducing CO_2 mobility in enhanced oil recovery (EOR) and CO_2 storage processes. CO_2 foam for mobility control can improve reservoir sweep efficiency, mitigate gravity override, and reduce viscous fingering for increased oil recovery (Enick et al. 2012) and CO_2 storage potential (Føyen et al. 2020). Foam is a thermodynamically unstable two-phase system of dispersed gas bubbles separated by continuous aqueous films (lamellae), stabilized by a foaming agent such as surfactant and/or nanoparticles. The geometry of the foam bubbles are dictated by the porous media they are contained within. Lamellae span entire pores, orthogonally to the general flow direction, reducing the mobility of gaseous phase. The aqueous phase remains continuous and is therefore unaffected by foam (Kovscek & Radke 1994). Despite successful field-scale tests (Alcorn et al. 2019; Blaker et al. 1999; Chou et al. 1992), others have been unsuccessful (Stephenson et al. 1993) due injectivity issues and difficulty attributing additional displacement specifically to CO_2 foam, which is related to a limited understanding of foam generation, flow dynamics, and coalescence at reservoir conditions. Therefore, this study aims to unlock real-time foam dynamics at high pressure (100 bar) by utilizing a realistic pore network with an extended field of view.

Population balance foam models provide a mechanistic framework where the kinetics of foam generation and coalescence is mathematically expressed to track the number of foam bubbles (Kovscek et al. 1995). The number of bubbles in the system is used to calculate the mobility of the gas , however, the calculation is not straightforward. Crucial input in the calculation must be estimated, which is challenging in opaque cylindrical core plugs and sand packs. Such input includes quantifying the trapped gas fraction (X_t), which requires dual gas-phase tracer measurements (Tang & Kovscek 2006). In addition, the texture of flowing foam bubbles (n_f), relies on measurements of produced foam which may not represent foam in porous media (Ettinger & Radke 1992; Hou et al. 2013).

Foam is generated in porous media by three main mechanisms, including *Roof snap-off*, *lamella mobilization/division and lamella leave-behind* (Ransohoff & Radke 1988; Rossen 2003;

Chen et al. 2005; Kovscek et al. 2007). The former two are considered prevailing mechanisms with lamellae orthogonal to flow direction and effective flow impediment (Kam & Rossen 2003). The third mechanism results in lamellae oriented parallel to flow direction, and an ineffective continuous gas foam (Friedmann et al. 1991; Kovscek & Radke 1994). Several studies have suggested that a minimum threshold pressure gradients (or minimum flow velocities) need to be exceeded for foam generation to be initiated (Ransohoff & Radke 1988; Rossen & Gauglitz 1990; Rossen et al. 1994; Gauglitz et al. 2002). The existence of minimum threshold pressure gradients can have unfavorable consequences for foam generation and propagation far from injection wells, where the pressure gradients are low. However, foam can be generated by *Roof snap off* independent of pressure gradients at sharp increases in permeability (Rossen 1999; Shah et al. 2019). During foam flow the pressure gradients can vary and fluctuate in space and time, resulting in local pressure gradients for the creation of lamellae (Kam & Rossen 2003). Positive feedback processes can also occur during foam generation because foam increases the pressure gradients and subsequently causes the generation of more foam (Føyen et al. 2020).

Foam coalescence reduces the number of bubbles in porous media by three mechanisms: coarsening by diffusion (Ostwald ripening), capillary suction drainage (Kovscek & Radke 1994) and gravitational liquid drainage. Coarsening by diffusion occurs due to the transport of gas from smaller bubbles (small radius, high curvature), with a higher internal pressure, to larger bubbles with lower internal pressure, causing the smaller bubbles disappear (Saint-Jalmes 2006; Marchalot et al. 2008). Capillary suction drainage occurs when the water saturation approaches a saturation value where the lamellae are no longer stable, because the capillary pressure exceeds the maximum disjoining pressure of the foam film and drains the lamellae (Jiménez & Radke 1989; Falls et al. 1989; Farajzadeh et al. 2015).

Gas mobility reduction by foam is caused by increased effective gas viscosity (μ_g^f) and decreased effective gas relative permeability (k_{rg}^f). The combined effect can be assessed by adapting Darcy's law for foam flow (Kovscek & Radke 1994).

$$u_g = \frac{k\, k_{rg}^f \nabla p_g}{\mu_g^f} \tag{1}$$

where u_g is the superficial gas flow velocity, k is the absolute permeability, k_{rg}^f is the effective gas-foam relative permeability, μ_g^f is the effective viscosity of flowing foam and ∇p_g is the gas pressure gradient.

Most quantification of foam strength relies on the measured pressure gradient. However, the pressure gradient depends on flow velocity (u) and absolute permeability (k), which lack generality, often making it unsuitable for comparison purposes. Foam apparent viscosity (μ_{app}) accounts for differences in absolute permeability and flow velocity and is commonly reported:

$$\mu_{app} = \frac{k}{u} * \nabla p_g \tag{2}$$

For foam flowing through the same pores where individual bubbles are constantly coalesced and regenerated (Ettinger & Radke 1992), the effective gas viscosity increases. The increased effective gas viscosity is caused by the viscous shear when lamellae move along pore walls (Hirasaki & Lawson 1985) and through pore throats (Falls et al. 1989). The effective viscosity of flowing foam (μ_g^f) is proportional to the bubble density (n_f) (Kovscek & Radke 1994; Fried 1961), and is typically shear-thinning with respect to interstitial velocity (v_f), and can be described by (Kovscek et al. 1995):

$$\mu_g^f = \mu_g + \frac{\alpha * n_f}{v_f^c} \tag{3}$$

where μ_g is the gas viscosity, $\alpha$is a system dependent scaling constant and $c$has been estimated to be approximately $1/3$ (Hirasaki & Lawson 1985).

In addition to increasing the effective gas viscosity, trapped foam reduces the gas-foam relative permeability (k_{rg}^f). The flowing bubble trains will occupy the largest pores (Radke & Gillis 1990) and a (Stone 1970) model for three-phase relative permeability is applicable to estimate the effective gas-foam relative permeability. By considering the flowing (S_{fg}) and trapped (S_{tg}) gas as two pseudo saturations, we have a three-phase system, with water as the third phase which is most wetting and the flowing gas-foam is the least wetting phase. The relative permeability of the least (and most) wetting phase depends only on its own saturation and is the same as its two-phase relative permeability. Therefore, the effective gas-foam relative permeability (k_{rg}^f) equals the no-foam gas relative permeability at the flowing gas saturation S_{fg} (Kovscek & Radke 1994).

The trapped gas fraction, X_t, is commonly used to compute the trapped gas saturation (S_{tg}) from gas saturation (S_g):

$$X_t = \frac{S_{tg}}{S_g} \tag{4}$$

Continuous-gas foam occurs when lamella generation becomes insufficient to maintain bubble densities, resulting in gas flow mainly through one or several interconnected channels not impeded by lamellae (Falls et al. 1989). The mobility reduction will be less compared to discontinuous foam because $n_f = 0$. However, the trapped bubbles will still reduce the mobility of the moving gas, as the gas-foam relative permeability (k_{rg}^f) is reduced.

Direct visual observation using microscopy during flow of fluids through porous media can be obtained using two-dimensional flow cells termed micromodels. Micromodels allow observation and characterization of individual fluid bubbles or ganglion and are particularly useful for foam studies for a range of important foam phenomena including generation (Géraud et al. 2017; Kovscek et al. 2007), coarsening (Jones et al. 2018a; Marchalot et al. 2008), texture (Rognmo et al. 2019; Rangel-German & Kovscek 2006), gas trapping (Lv et al. 2018; Jones et al. 2018b), flow (Géraud et al. 2016) and flow diversion (Khoshkalam et al. 2019; Gauteplass et al. 2015). Most microfluidic studies investigated decoupled foam phenomena in a limited field of view (FoV), whereas a complete assessment of foam in porous media requires combined observations of foam generation, coarsening, and texture.

This work presents a comprehensive laboratory investigation of essential foam features and phenomena during dynamic flow at reservoir conditions over a representative area, supported by the framework developed for population balance foam models. In addition, we investigate the foam generation and stabilization when adding nanoparticles at two different concentrations (150 and 1500 ppm) to the foaming solution.

2 Materials and Methods

2.1 Fluid preparation

Brine (3.5 wt.% NaCl) was used for all aqueous phases (Table 1) and was filtered through a 0.45 µm cellulose acetate filter to remove particles before mixing with other components or injected it through the micromodel. Two foaming agents were used: Surfonic L24-22A (a non-ionic surfactant with linear ethoxylated alcohol, Huntsman), and Levasil CC301 (a surface-modified spherical silica nanoparticle, Nouryon). Three foaming solutions were prepared by mixing brine with surfactant, nanoparticle or a hybrid combination of both (Table 1). CO_2 of 99.999% purity was used during the micromodel foam injections. The pore space was cleaned between each injection cycle using 2-propanol-water azeotrope (IPA).

Table 1 Composition of aqueous solutions.

Aqueous Solution	**Concentration,** *Component*
Brine	**35000 ppm,** *NaCl in distilled water*
SF5000	**5000 ppm,** *Surfonic L24-22*
SF5000 + NP1500	**5000 ppm,** *Surfonic L24-22,* + **1500 ppm,** *Levasil CC301*
SF5000 + NP150	**5000 ppm,** *Surfonic L24-22,* + **150 ppm,** *Levasil CC301*
IPA	**877000 ppm,** *2-propanol in distilled water*

2.2 Micromodel and holder

The micromodel consists of an etched silicon wafer with a realistic porous structure bonded to an optically transparent borosilicate glass. The chemical characteristics of crystalline silicon (silicon wafer) and borosilicate glass are similar to sandstone (mainly quartz), which are chemically inert to injected fluids. Deep reactive ion etching resulted in vertical pore walls and sharp edges, resembling grain shapes found in real reservoir rocks generated from Berea sandstone thin sections. However, when 3D porous media in a real reservoir rock is simplified to 2D, some modifications were made to the pattern to connect pores which were isolated, resulting in higher permeability and porosity relative to Berea sandstone. Complete production procedures can be found in (Buchgraber et al. 2012). The rectangular porous pattern (27 mm X 21.40 mm) was equipped with flow ports in each corner, with inlet and outlet fluid distribution channels (200 μm width) that connected ports 1 and 2, and ports 3 and 4 (**Figure 1**). The porous pattern (27000 grains) constitutes 36 (4 x 9) repetitions of pore network with 749 unique grains with shapes from a thin-section image of natural sandstone; a rock type extensively used in laboratory studies of oil production, foam and CO_2 storage. The porous pattern can be considered as a simplified two-dimensional projection of real pore structures, with connected pores that allow flow and discontinuous, irregularly shaped grains that provide flow tortuosity.

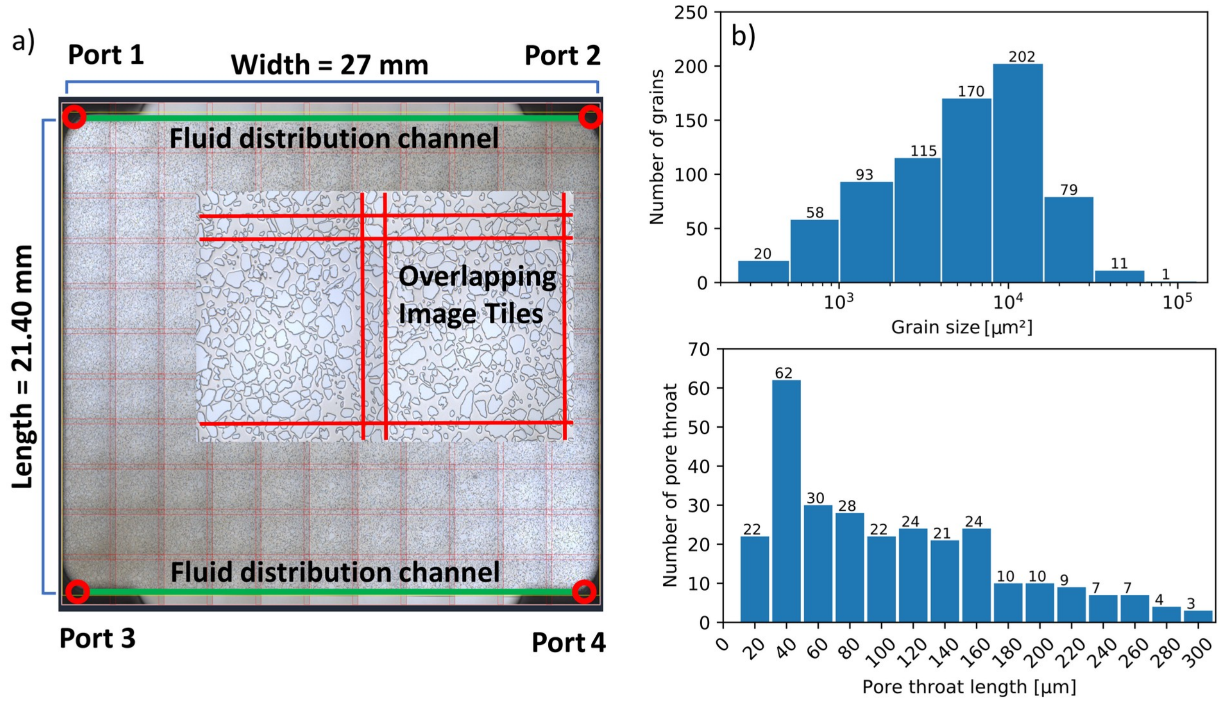

Fig. 1 Right: Dimensions of porous pattern in micromodel, location of flow ports and fluid distribution channels. The overlapping image acquisition titles (121 in total) are shown using red lines above the porous pattern (exaggerated for illustration purposes). Left: Characteristic features of the micromodel from one of the 36 repetitions of the pattern, grain size distribution (top) and pore throat length distribution (bottom). Average pore throat length was 89 µm.

Micromodel properties are listed in Table 2. The porosity was quantified as the ratio of areal pore space to the total area (grains + pore space) and was calculated to be 0.61 from a stitched, high-resolution images of the whole porous pattern. The pore volume (PV) with constant etching depth of 30 μm was 11.1 μL. The grain size distribution of the unique pattern with 749 grains ranged between 100 to 79 000 μm^2 and the pore throat (defined as the shortest pore space distance between two adjacent grains) distribution ranged between 10 to 200 μm (**Figure 1**). The constant etching depth resulted in square- or rectangular-shaped pore throat cross-sections. The absolute permeability of the micromodel was 2.97 D.

Table 2 Micromodel properties.

Parameter	Value
Width	27 mm
Length	21.40 mm
Depth	30 μm
Porosity	0.61
Permeability	2.97 D
Pattern repetition	36
Unique grains	749
Total grains	27000
Grain size	100-79000 μm^2
Pore throat length	10-200 μm

The micromodel was positioned in a depression in the bottom part of the two-part aluminum micromodel holder with flow ports aligned with threaded connections sealed with O-rings. The top part, with an open window for direct observation, was attached to the bottom with eight screws using 0.20 Nm force. The system can be pressurized to 150 bar without external confinement pressure.

2.3 Experimental setup and procedure

The micromodel holder was positioned on a motorized scanning stage below the microscope (Axio Zoom. V16, Zeiss) equipped with a diffuse ring-illuminator. The microscopic zoom, focus, illuminator intensity, imaging, and the motorized stage was controlled with the Zeiss proprietary software. Microscope settings (light intensity, aperture and shutter time) were optimized for image processing and kept constant for all experiments. The software performed shading corrections and focus adjustments for any misalignments. Fluid injection and production utilized a series of valves and pumps (**Figure 2**) and the pore pressure was kept at a minimum of 100 bar using a backpressure system. The injected and produced fluids were considered incompressible at the system temperature (ambient), and pressure gradients during flow (tens of millibars) were not expected to change fluid properties and flow rates. Four unsteady state CO_2 injections were performed (three with foaming solutions listed in Table 1, and one using brine for baseline) using the following procedure:

i. Pre-saturate the micromodel with foaming solution

ii. Inject dense phase CO_2 at a constant volumetric flow rate (4 $\mu L/min$) into port1 with port 2 closed and ports 3 and 4 open and kept at 100 bars using the backpressure system.

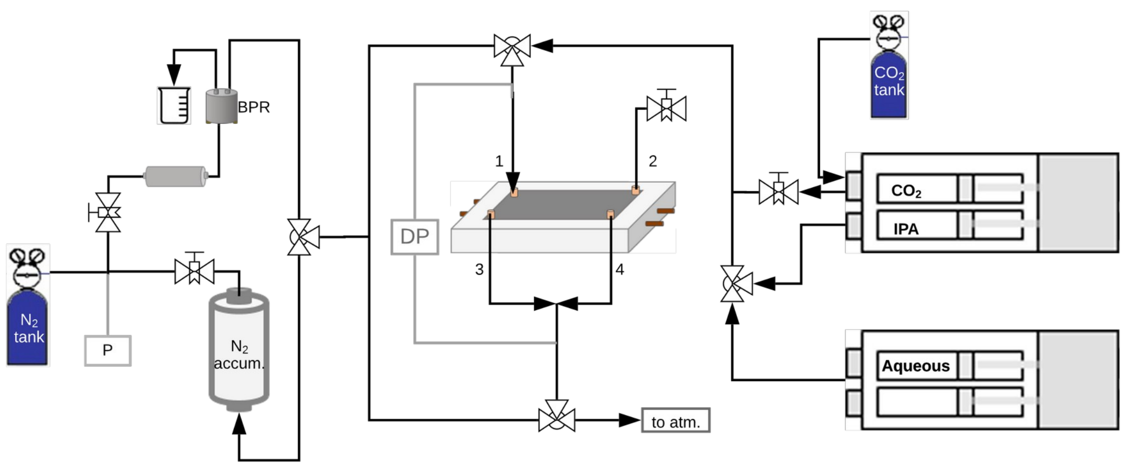

Fig. 2 Experimental setup used for the pore-scale foam studies using etched-silicon wafer micromodels. The micromodel holder was positioned underneath the microscope (not shown). Two high precision plunger pumps (Quizix Q5000-2.5K and Quizix Q5000-10K) were used for fluid injection. The Q5000-2.5K pump was used in single cylinder injection mode, with CO_2 and cleaning solvents (IPA) in each of the two cylinders, whereas the Q5000-10K was solely used for injection of surfactant. The N_2 accumulator tank was used to regulate the backpressure: a 1 L pressure vessel was filled with N_2 and received the produced fluids (water and dense liquid CO_2) during injections. The produced fluids were vented from the pressure vessel during the preparation between the micromodel foam experiments.

2.4 Image processing and analysis

The motorized scanning stage and software enabled imaging of the entire porous pattern (27 mm X 21.40 mm) with high spatial resolution (4.38 μm/pixel) by stitching multiple overlapping images (**Figure 1**). Image acquisition time of the porous pattern (121 separate images) was 1 min 13 sec and time-lapsed series captured the position of each individual foam bubble every 1 min 15 sec. The following three-step image segmentation process was performed:

i. Thresholding the images using a low (dark) threshold value by utilizing the significantly darker colored grain structure compared to the pore space. The grains were then drawn black on a white empty image.
ii. Thresholding the images using a high (bright) threshold value by utilizing the white colored (due to the diffuse ring-illuminator) gaseous-aqueous interfaces and grain walls. The bright areas were then painted black on the white empty image.
iii. The rest of the white empty image is the discrete bubbles. This resulted in a binary image with grains, grain walls and gaseous-aqueous interfaces as black, and discrete bubbles as white.

The final segmented image (**Figure 3**) shows the discrete bubbles colored red and grains colored blue for illustrative purposes. The bubbles were further described using functions available in the Python library OpenCV (Bradski 2000) as continuous contours with the following features: center of mass (coordinates), area, perimeter length, orientation, bounding boxes, and minimum enclosing ellipse with minor and major axis. These characteristics were used in the analysis of foam flow and bubble generation/coalescence.

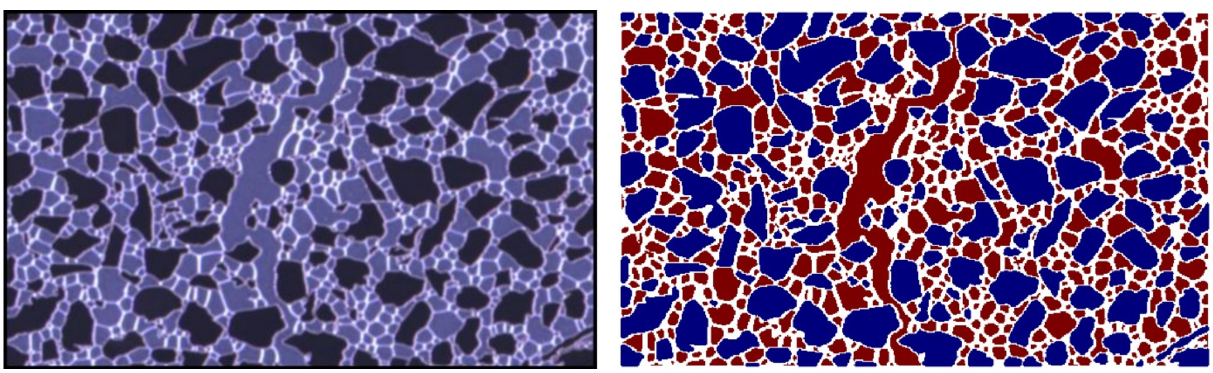

Fig. 3 Illustration of the segmentation process. Left: Raw image (2.2 mm x 1.3 mm) of the micromodel with foam occupying the porous pattern. Right: Segmented image, blue areas are the grain structure, red areas are discrete foam bubbles

3 Results and discussion

Pore-scale foam flow phenomena were studied using temporal bubble density mapping, bubble number (N_i) and bubble size during foam generation and coalescence. Temporal bubble numbers during foam generation and coalescence (N_{bubble}) were normalized to the baseline ($N_{baseline}$) for three foaming solutions (**Figure 4**). Foam generation increased N to approximately 90 to 100 times of the baseline, reaching peak values after approximately 5 PV of CO_2 injected. Bubble coarsening (decreased N) was the dominating coalescence mechanism. The foam generation and stabilization were not affected by adding nanoparticles to the foaming solution as the temporal bubble numbers for the three injections had same trend. Detailed discussion of results from foam generation (3.1), foam flow (3.2), and foam decay (3.3) is below.

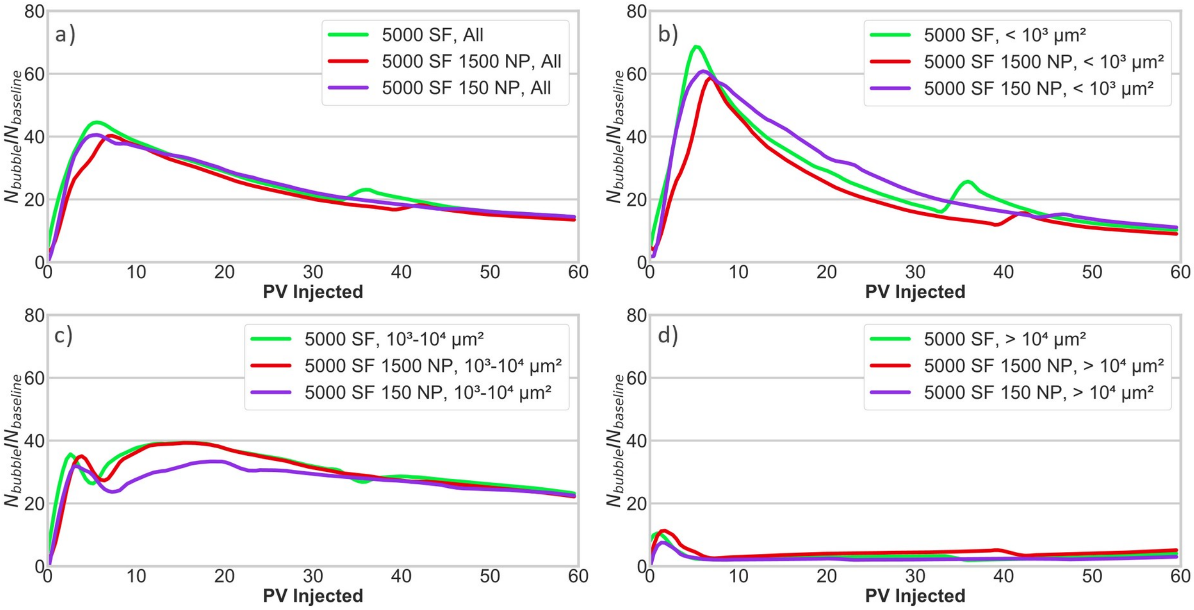

Fig. 4 Development in normalized bubble number (with respected to the baseline). The bubbles are sorted into logarithmical bubble size groups: a) all bubbles; b) <u>small</u> bubbles with area ¿ $10^3 \mu m^2$; c) <u>intermediate</u> bubbles with area between 10^3 ¿ $10^4 \mu m^2$; d) <u>large</u> bubbles with area ¿ $10^4 \mu m^2$. Sorting the number of bubbles based on size shows that the number of intermediate size bubbles are increasing at the expense of small bubbles after 5 PV of CO_2 injection. The baseline and the foam injections are smoothed with a running average of 51 and 11, respectively.

<u>3.1 Foam generation</u>

Foam generation occurred primarily by snap-off in regions with sufficient liquid saturation and sharp constrictions between pore throats and bodies. Subsequent flow diversion increased CO_2 flow velocity locally, resulting in additional foam generation. Bubble density maps initially show low foam generation with a rapid increase when the injected CO_2 reached the outlet flow channel between 0.4 and 1.3 PV CO_2 injected (**Figure 5**). This resulted in backward (from outlet to inlet) foam propagation; previously reported and attributed to foam becoming stronger (Simjoo & Zitha 2020; Almajid et al. 2019; Apaydin & Kovscek 2001). The determining mechanisms for foam strengthening are not clear, and it has hypothesized to occur by foam transitioning from weak to strong state, or by favorable conditions for snap-off in the transition zone. We cannot rule out or support either hypotheses. Backward propagation of the foam front does, however, indicate that snap-off was the prevailing generation mechanism during the initial period because lamella mobilization and division is a secondary generation mechanism that requires the presence of foam and can only result in forward-propagation. The secondary generation mechanism may have contributed to refinement of the foam texture and regeneration to increase bubble densities after the initial period. The observed foam behavior is likely important for long-distance foam generation where pressure gradients are likely to be small (Hirasaki et al. 1997; Szafranski et al. 1998). Foam generation at sharp permeability contrasts can also occur some distance from the injection well at lower pressure gradients if sufficient foaming solutions are available. Additionally, super-linear increases in apparent viscosity during core scale unsteady state experiments, indicate that positive feedback behavior (Føyen et al. 2020) is likely related to the backward propagation mechanism observed at the pore-level**.**

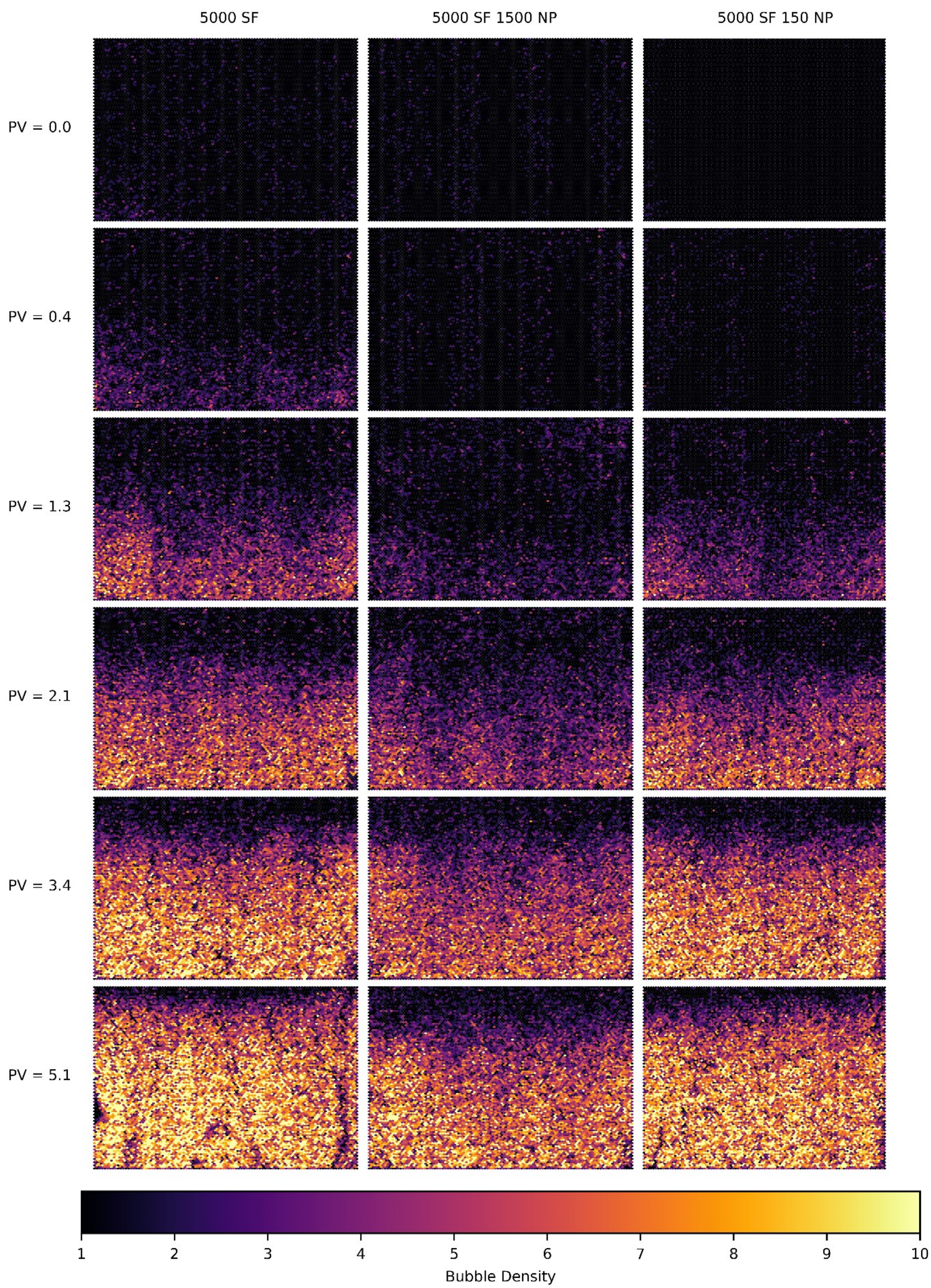

Fig. 5 Bubble density mapping during foam generation (up to 5 PV of CO_2 injection) for three foam solutions listed

in Table 1. Foam generation initiated between 0.4 and 1.3 PV of CO_2 injected at the sharp permeability contrast (outlet flow channel, bottom side of density maps), resulting in higher foam density (brighter color) in the outlet regions of porous pattern. Foam propagated backwards (outlet to inlet) resulting in higher foam density through the micromodel. The resolution of the spatially resolved hexagonal binning plot is 150 X 90.

3.2 Flowing and trapped foam

Flowing regions were characterized by moving bubble trains and continuous gas channels. Movement of bubble trains occurred with temporary flow suspension, restart and randomly relocated (**Figure 6**). Open gas channels extended several pore lengths and emerged from inadequate upstream bubble regeneration to replace displaced bubbles downstream. Open channels were irregularly filled with bubbles and reemerged in the same or new pathways. Trapped bubbles adjacent to open or partially filled channels changed from low energy configuration (no curvature, image a) to texture with less capillary resistance (with curvature, images c and f). The observation of large regions of trapped bubbles support that lamellae moving to a minimum energy configuration (at rest) will have a greater capillary resistance to remobilization (Jones et al. 2018a; Hou et al. 2013). Hence, the lamella in stationary regions will not move when exposed to the same pressure gradient as the lamella in the flowing region.

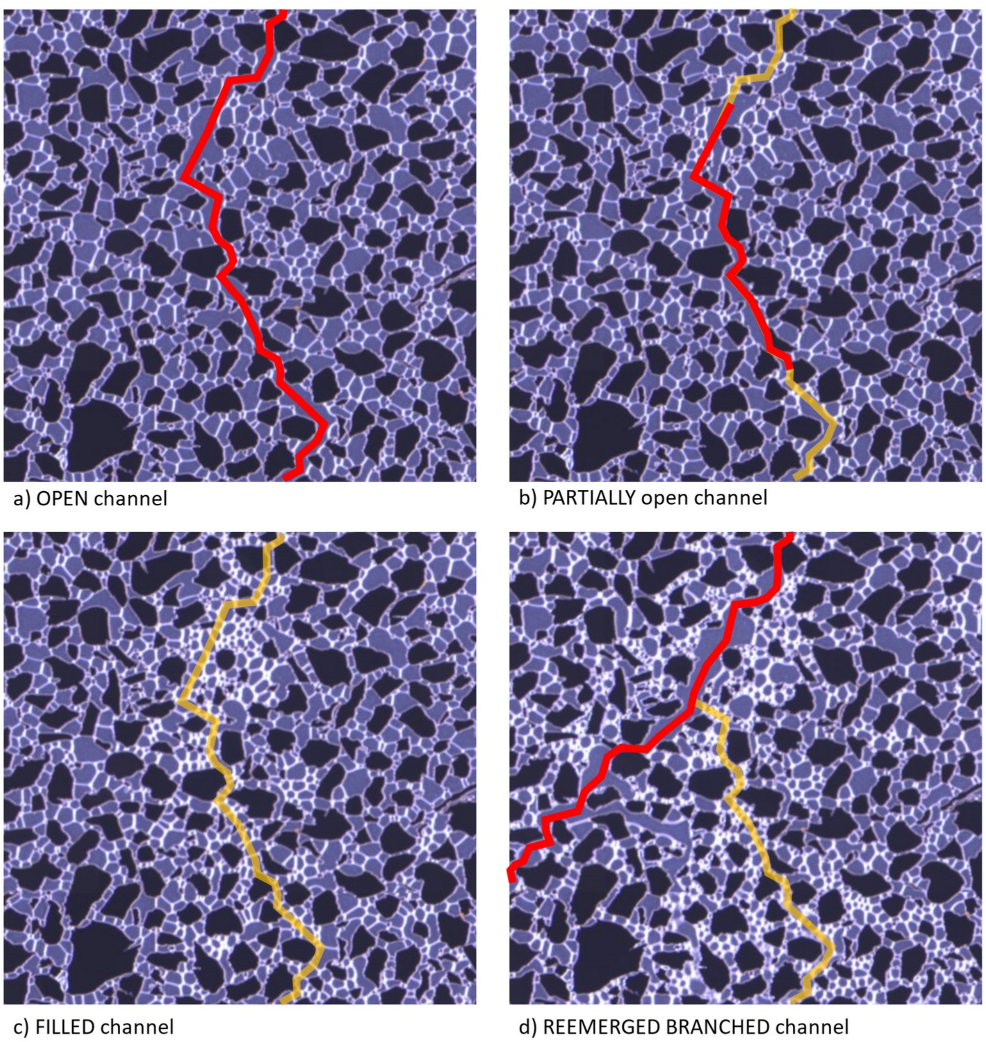

Fig. 6 Dynamics of open gas channels during bubble generation: red indicates path of an open channel (without bubbles) and orange indicates where the open channel fills with bubbles. Sequential images show: a) path of an open channel (t = 33.8 PV); b) channel becomes partially open (t = 34.2 PV); c) channel becomes filled with bubbles (t = 34.7 PV); d) a new path emerges that branches from the original path, now partially filled with bubbles (t = 35.1 PV). The images are from the SF5000 injection at the same field of view (2.2 mm x 2.2 mm).

The density of the flowing bubbles (n_f) is used to calculate the effective gas viscosity in population balance foam models and is commonly assumed to be equal to the density of trapped bubbles (n_t) (Kovscek and Radke 1994). With a limited field of view (2 mm x 2 mm, **Figure 6**), assessment of local n_f becomes ambiguous:

i. In open channels (images a and d), the CO_2 flow is not impeded by bubbles and $n_f = 0$, *i.e.* $n_f < n_t$
ii. In filled channels (image c, n_f is higher than n_t in surrounding region, *i.e.* $n_f > n_t$
iii. Partially filled channels (image b), n_f is the mean value of the filled and the open part of the channel, and depends on the relative size between the two parts and the bubble density

Hence, a foam representative elementary volume (foam-REV) must be defined that provides a n_f representative for the whole system (Hill 1963). Dynamics of bubble density, gas channels, flowing bubbles and trapped bubbles were therefore mapped in the entire pore space using hexagonal binning plot (**Figure 7**). Open gas channels were defined as large bubbles exceeding a size of 25% of micromodel length. Flowing bubbles were identified by temporal changes in bubble position and size, individually determined for all bubbles: bubble position changed if the relocation exceeded 20% of its minor axis (defined by an enclosing eclipse) between time-lapse images, and bubble size changed if its area increased/decreased more than 20%. Temporal changes in bubble position and size and the position of open gas channels were based on observations between 5 image frames, corresponding to 1.7 PV CO_2 injected. Trapped bubbles (without change in position and size) were found by combining the bubble density and flowing bubble maps: *trapped = density / (flow +1)*. It is not known if the size of the whole porous pattern (27 mm x 21.40 mm) is sufficient to define foam-REV. Still, we observed that the length of the open channels remained constant for extended periods (**Figure 8**). Therefore, when the relationship between flowing and stationary regions is constant, we can estimate a mean representative flowing bubble density.

The gas mobility in the presence of foam can be found with knowledge of trapped bubbles (reduced gas relative permeability) and moving bubble trains (increased effective gas viscosity). The latter can be ignored when open gas channels spanned the porous pattern (Equation 3 ($n_f = 0$) $\rightarrow \mu_g^f = \mu_g = 0.081 cP$). Hence, gas mobility can be determined directly from the fraction of trapped gas (X_t), that is estimated from the open gas channel area (**Figure 8**) or flowing region area (**Figure 7**). Note that the flowing regions were determined over 1.7 PV and the fraction of trapped bubbles is underestimated due to the irregular relocation of bubble trains and continuous gas channels (**Figure 7**). The gas mobility can be determined when the majority of flow occurs in open gas channels because they can be used to estimate X_t by subtracting the volume (area) constituting the open gas channels (**Figure 8**): with open gas channels occupying between 0.75 to 1.75% of the pore space, X_t ranged between 0.98 and 0.99 (assuming S_g = 0.8). As mentioned earlier, the effective gas-foam relative permeability equals the no-foam gas relative permeability at the flowing gas saturation, and by assuming a linear relationship between relative permeability and saturation, the gas-foam relative permeability (k_{rg}^{f}) can be calculated to range between 0.008 and 0.016. Foam apparent viscosity has been calculated using equation 1 and 2 to range between 5.1 to 10.1 cP that corroborates core floods at similar conditions (Føyen et al. 2020).

The effective gas viscosity from bubble trains cannot be ignored when open gas channels do not span the porous pattern and must be taken into account to assess the gas mobility reduction for such cases using Equation 1. Direct quantification is not obtainable from the images because the parameter α that depends on the foaming system and germination sites (Pancharoen et al. 2012) cannot be estimated from the unsteady state injections reported here. However, adequate measured differential pressure can potentially be used to estimate α, which is a parameter used in population balance modeling (Kovscek et al. 1995; Eide et al. 2020). Direct quantification of α by micromodel studies can, therefore, be valuable for foam agent screening, as it is less time consuming than core floods, and can be used as input for population balance modeling.

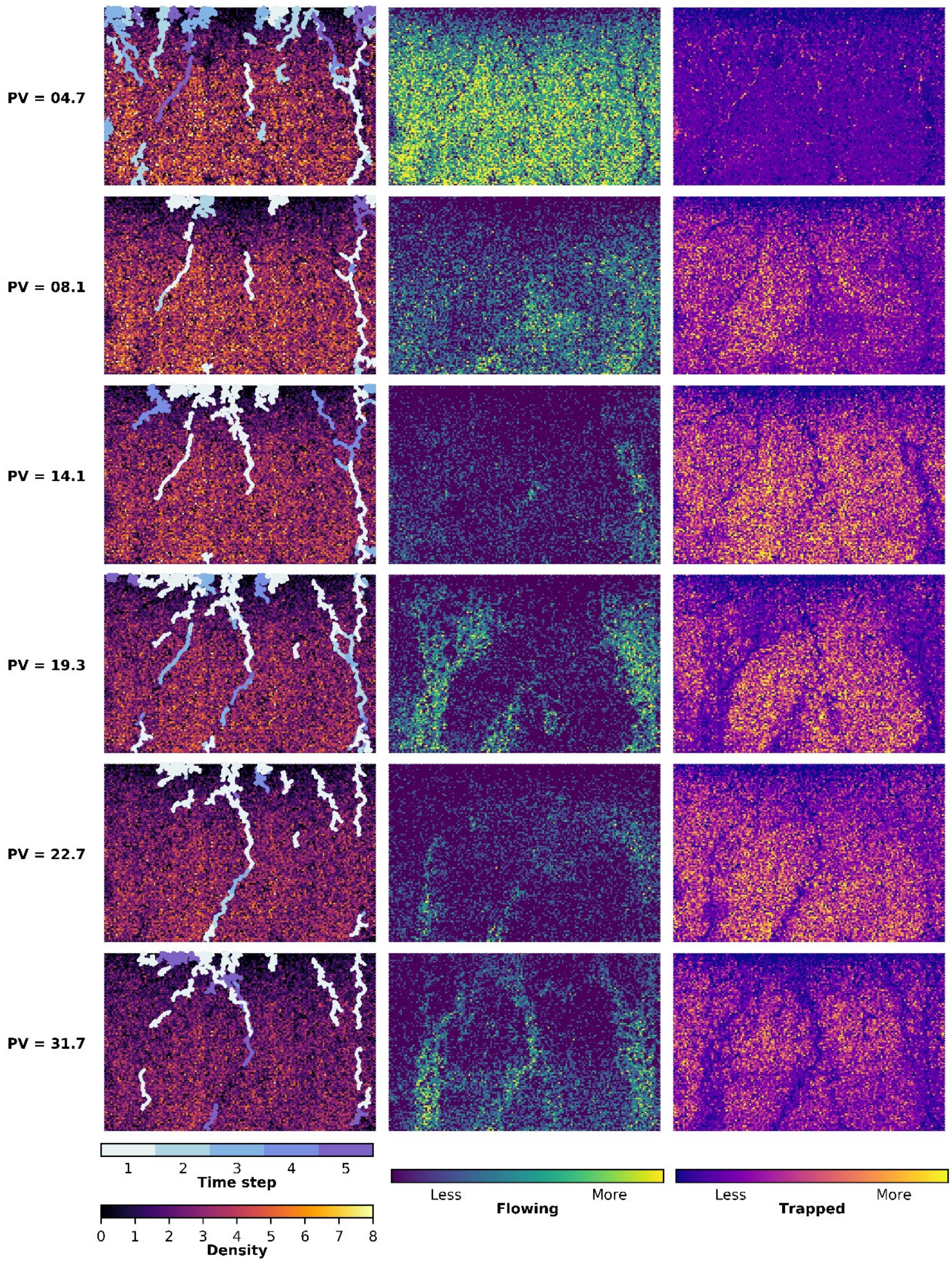

Fig. 7 Pore-scale foam dynamics with spatial bubble density, open gas channels, flowing bubbles and trapped bubbles using hexagonal binning plots (150 x 90) Left column: bubble density (number of bubbles in each hexagon) with mapped open gas channels (lines). Center column: flowing bubbles. Right column: Trapped bubbles. Location of open gas channels, flowing and trapped bubbles were calculated each 1.7 PV CO_2 injected. The micromodel was pre-saturated with the foaming solution (SF5000) prior to CO_2 injection (top to bottom)

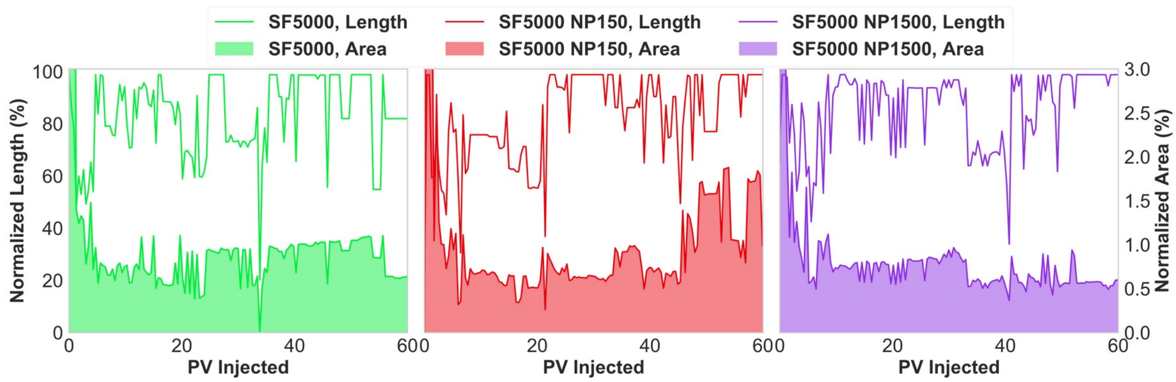

Fig. 8 Quantification of open gas channel length and area for three foaming solutions. The length is normalized between inlet (0%) and outlet (100%) using solid lines. Channel area (filled region) is normalized to pore space when the channel length exceeds 25%

3.3 Foam decay

Foam coalescence became dominant at later times (after approximately 5 PV of CO_2 injected, **Figure 4**) with overall decreasing bubble numbers. We rank coalescence mechanisms in our porous media from the three known bubble coalescence mechanisms: *i.* coarsening by diffusion (Ostwald ripening), *ii.* liquid film drainage by capillary or gravity forces, and *iii.* gravitational liquid drainage. From the observed flow pattern changes due to foam regeneration (discussed in detail below) we conclude that capillary liquid film drainage is not prevailing because it requires low liquid saturations not consistent with observations. Gravitational liquid drainage is considered negligible in the horizontally oriented system with 30 μm etching depth. Therefore, we consider Ostwald ripening the prevailing coalescence mechanism, where intermediate-sized bubbles increased at the expense of smaller bubbles (**Figure 4**). Smaller bubbles disappeared due to diffusive gas transport from bubbles with higher Laplace pressure (small bubble radii) to bubbles with lower Laplace pressure (high bubble radii). Fick's law determines diffusion rate, and it is expected that Ostwald ripening will depend on time. The development in bubble number and mean bubble area (A) agrees with Von Neumann's law (Saint-Jalmes 2006; Marchalot et al. 2008) that describes coarsening in trapped two-dimensional foam (**Figure 9**). The development in mean bubble area and the ratio $N_o/N(t)$ scales linearly with time (PV injected), where $N(t)$ is the number of bubbles at a time t and N_0 is the initial number of bubbles before foam coalescence becomes dominant. N_o is the greatest observed bubble number and marked the transition between when the rate of foam coalescence exceeded rate of foam generation. The transition can be recognized when $N_o/N(t)=1$ (after approximately 5 PV CO_2 injected), and the relationship $N_o/N(t)$ increases as the foam texture becomes coarser. We focus our foam coarsening analysis between 5 and 30 PV injected as foam was regenerated between 35 and 45 PV injected, likely caused by mobilization of foaming solution from system dead ends.

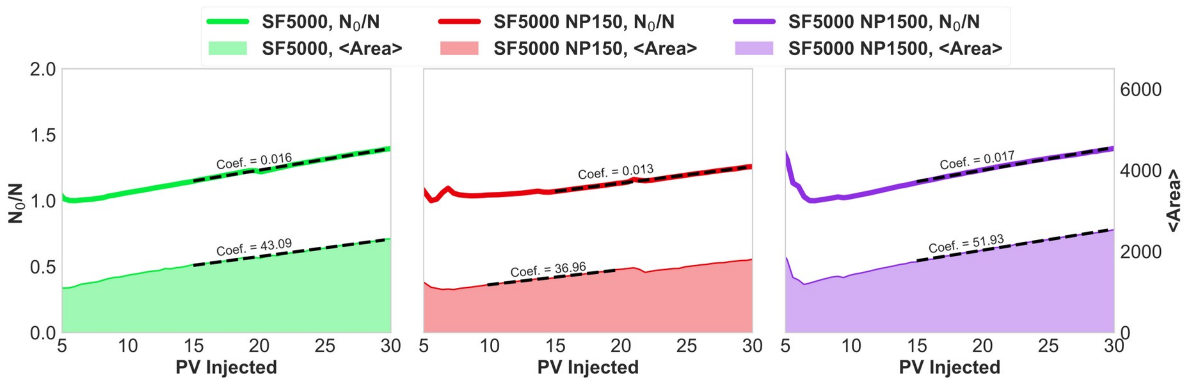

Fig. 9 Increasing $N_o/N(t)$ with decreasing number of bubbles (*left axis, solid line*) and increasing mean bubble area ¿ A>¿ (*right axis, filled area*) during foam coalescence by Ostwald ripening for three foaming solutions. Both the mean bubble area and the ratio $N_o/N(t)$ scaled linearly with time (PV injected) and agrees with Von Neumann's law for two-dimensional foams. The associated regression coefficient (slope) are included on top of the curves

In trapped, two-dimensional foams, coarsening is expected to stop when foam lamellae are located at the pore-throats with zero curvature, *i.e.* equal bubble pressures without pressure gradients to drive further diffusion and coarsening (Jones et al. 2018a). Hence, A and $N_o/N(t)$ scale with time only during a limited initial coarsening period (Jones et al. (2018a) reported 1500 sec), before the lamellae come to rest at the pore throats. The presence of large gas channels and slow foam regeneration sustained foam coarsening from approximately 5 PV CO_2 injected. The presence of large gas channels spanning several pores observed in our system (**Figure 9**) were effectively large bubbles with lower pressure than surrounding bubbles that promoted sustained Ostwald ripening. The prolonged coarsening caused the mean bubble areas for the three injections to increase in an average sense as 44 μm^2 per PV injected over minimum 25 PV (4125 sec). The rate of increase was 0.26 $\mu m^2 s^{-1}$, compared with 1.14 $\mu m^2 s^{-1}$ for two-dimensional trapped foam during a limited initial coarsening period (Jones et al. 2018a). The difference between stationary and flowing systems is expected as regeneration of foam does not occur in a stationary system. Additionally, different gases and pressures were used, and the solubility of the gaseous phase in aqueous phase influence diffusion and subsequent coarsening.

4 Conclusions

Bubble flow, texture and trapping dynamics for dense CO_2 foam were studied at high pressure at the pore scale using a realistic pore network. The aggregated effect of foam generation, coarsening, and texture was contextualized through the population balance model framework. Roof snap-off at sharp permeability contrasts was the dominant foam generation mechanism with additional refining of foam texture caused by backward foam propagation. Coarsening during continuous CO_2 injection occurred due to Ostwald ripening. Foam generation and stabilization were not affected by adding nanoparticles to the foaming solution. Flowing regions were characterized by moving bubble trains and open gas channels. Stationary regions with trapped foam had a greater capillary resistance than moving bubble trains. The gas mobility in the presence of open gas channels and trapped bubbles was estimated by quantifying the fraction of trapped bubbles, corresponding to an apparent foam viscosity between 5.1 to 10.1 cP. Assessment of foam texture (n_f and n_t) needs to be performed over a significantly large area of the porous pattern to define a foam representative elementary volume.

5 Data availability

The foam injection datasets, including segmented images, used during the current sturdy are available at http://dx.doi.org/10.17632/5d37nbzf9s.1, an open-source online data repository hosted by Mendeley Data (Benali & Føyen 2020). The raw foam injection micromodel images are available from the corresponding author on reasonable request.

6 Abbreviation and Nomenclature

Carbon dioxide	CO_2
field of view	FoV
PV	Pore volume
foam representative elementary volume	foam-REV
Permeability	k
Effective gas-foam relative permeability	k_{rg}^{f}
Gas viscosity	μ_g
Effective viscosity of flowing foam	μ_g^f
Superficial gas flow velocity	u_g
Foam apparent viscosity	μ_{app}
Gas pressure gradient	∇p_g
Gas saturation	S_g
Flowing gas saturation	S_{fg}
Trapped gas saturation	S_{tg}
Flowing bubble density	n_f
Trapped bubble density	n_t
Total number of bubbles	N_{bubble}
Baseline number of bubbles	$N_{baseline}$
Initial number of bubbles before foam coalescence	N_o
mean bubble area	A

trapped gas fraction	X_t
System dependent scaling constant	α

7 Acknowledgements

The authors wish to acknowledge the Research Council of Norway for financial support (project no. 249742, 268216, 294886 and 301201) for funding of PhD candidate Benyamine Benali and Dr. Zachary Paul Alcorn, and support from industry partners Nouryon, Shell E&P, Total E&P, and Equinor.

8 References

Alcorn, Z. P., Fredriksen, S. B., Sharma, M., Rognmo, A. U., Føyen, T. L., Fernø, M. A., & Graue, A. (2019). An Integrated Carbon-Dioxide-Foam Enhanced-Oil-Recovery Pilot Program With Combined Carbon Capture, Utilization, and Storage in an Onshore Texas Heterogeneous Carbonate Field. SPE Reservoir Evaluation & Engineering, 22(04), 1449-1466. doi:10.2118/190204-pa

Almajid, M.M., Nazari, N., Kovscek, A.R.: Modeling Steady-State Foam Flow: Hysteresis and Backward Front Movement. Energy & Fuels (2019). https://doi.org/10.1021/acs.energyfuels.9b01842

Apaydin, O.G., Kovscek, A.R.: Surfactant Concentration and End Effects on Foam Flow in Porous Media. Transport in Porous Media (2001). https://doi.org/10.1023/A:1010740811277

Benali, B., Føyen, T.: [Dataset] Micromodel foam.... In. Mendeley Data, (2020)

Blaker, T., Celius, H.K., Lie, T., Martinsen, H.A., Rasmussen, L., Vassenden, F.: Foam for Gas Mobility Control in the Snorre Field: The FAWAG Project. Paper presented at the SPE Annual Technical Conference and Exhibition, Houston, Texas, 1999/1/1/

Bradski, G.: The opencv library. Dr Dobb's J. Software Tools **25**, 5 (2000)

Buchgraber, M., Al-Dossary, M., Ross, C.M., Kovscek, A.R.: Creation of a dual-porosity micromodel for pore-level visualization of multiphase flow. Journal of Petroleum Science and Engineering (2012). https://doi.org/10.1016/j.petrol.2012.03.012

Chen, M., Yortsos, Y.C., Rossen, W.R.: Insights on foam generation in porous media from pore-network studies. Colloids and Surfaces A: Physicochemical and Engineering Aspects (2005). https://doi.org/10.1016/j.colsurfa.2005.01.020

Chou, S., Vasicek, S., Pisio, D., Jasek, D., Goodgame, J.: CO2 Foam Field Trial at North Ward-Estes. Paper presented at the SPE Annual technical conference and exhibition,

Eide, Ø., Fernø, M., Bryant, S., Kovscek, A., Gauteplass, J.: Population-balance modeling of CO2 foam for CCUS using nanoparticles. Journal of Natural Gas Science and Engineering (2020). https://doi.org/10.1016/j.jngse.2020.103378

Enick, R.M., Olsen, D.K., Ammer, J.R., Schuller, W.: Mobility and Conformance Control for CO2 EOR via Thickeners, Foams, and Gels -- A Literature Review of 40 Years of Research and Pilot Tests. Paper presented at the SPE Improved Oil Recovery Symposium, Tulsa, Oklahoma, USA, 2012/1/1/

Ettinger, R.A., Radke, C.J.: Influence of Texture on Steady Foam Flow in Berea Sandstone. SPE Reservoir Engineering (1992). https://doi.org/10.2118/19688-PA

Falls, A.H., Musters, J.J., Ratulowski, J.: The Apparent Viscosity of Foams in Homogeneous Bead Packs. SPE Reservoir Engineering (1989). https://doi.org/10.2118/16048-PA

Farajzadeh, R., Lotfollahi, M., Eftekhari, A.A., Rossen, W.R., Hirasaki, G.J.H.: Effect of Permeability on Implicit-Texture Foam Model Parameters and the Limiting Capillary Pressure. Energy & Fuels (2015). https://doi.org/10.1021/acs.energyfuels.5b00248

Fried, A.N.: Foam-Drive Process for Increasing the Recovery of Oil. In. University of North Texas Libraries, Washington D.C., (1961)

Friedmann, F., Chen, W.H., Gauglitz, P.A.: Experimental and Simulation Study of High-Temperature Foam Displacement in Porous Media. SPE Reservoir Engineering (1991). https://doi.org/10.2118/17357-PA

Føyen, T., Brattekås, B., Fernø, M.A., Barrabino, A., Holt, T.: Increased CO2 storage capacity using CO2-foam. International Journal of Greenhouse Gas Control (2020). https://doi.org/10.1016/j.ijggc.2020.103016

Gauglitz, P.A., Friedmann, F., Kam, S.I., Rossen, W.R.: Foam generation in homogeneous porous media. Chemical Engineering Science (2002). https://doi.org/10.1016/S0009-2509(02)00340-8

Gauteplass, J., Chaudhary, K., Kovscek, A.R., Fernø, M.A.: Pore-level foam generation and flow for mobility control in fractured systems. Colloids and Surfaces A: Physicochemical and Engineering Aspects (2015). https://doi.org/10.1016/j.colsurfa.2014.12.043

Géraud, B., Jones, S.A., Cantat, I., Dollet, B., Méheust, Y.: The flow of a foam in a two-dimensional porous medium. Water Resources Research (2016). https://doi.org/10.1002/2015wr017936

Géraud, B., Méheust, Y., Cantat, I., Dollet, B.: Lamella Division in a Foam Flowing through a Two-Dimensional Porous Medium: A Model Fragmentation Process. Physical Review Letters (2017). https://doi.org/10.1103/PhysRevLett.118.098003

Hill, R.: Elastic properties of reinforced solids: Some theoretical principles. Journal of the Mechanics and Physics of Solids (1963). https://doi.org/10.1016/0022-5096(63)90036-X

Hirasaki, G.J., Lawson, J.B.: Mechanisms of Foam Flow in Porous Media: Apparent Viscosity in Smooth Capillaries. Society of Petroleum Engineers Journal (1985). https://doi.org/10.2118/12129-PA

Hirasaki, G.J., Miller, C.A., Szafranski, R., Tanzil, D., Lawson, J.B., Meinardus, H., Jin, M., Londergan, J.T., Jackson, R.E., Pope, G.A., Wade, W.H.: Field Demonstration of the Surfactant/Foam Process for Aquifer Remediation. Paper presented at the SPE Annual Technical Conference and Exhibition, San Antonio, Texas, 1997/1/1/

Hou, J., Du, Q., Li, Z., Pan, G., Lu, X., Zhou, K.: Experiments on foam texture under high pressure in porous media. Flow Measurement and Instrumentation (2013). https://doi.org/10.1016/j.flowmeasinst.2013.05.002

Jiménez, A.I., Radke, C.J.: Dynamic Stability of Foam Lamellae Flowing Through a Periodically Constricted Pore. In: Oil-Field Chemistry, vol. 396. ACS Symposium Series, vol. 396, pp. 460-479. American Chemical Society, (1989)

Jones, S.A., Getrouw, N., Vincent-Bonnieu, S.: Foam flow in a model porous medium: I. The effect of foam coarsening. Soft Matter (2018a). https://doi.org/10.1039/C7SM01903C

Jones, S.A., Getrouw, N., Vincent-Bonnieu, S.: Foam flow in a model porous medium: II. The effect of trapped gas. Soft Matter (2018b). https://doi.org/10.1039/C7SM02458D

Kam, S.I., Rossen, W.R.: A Model for Foam Generation in Homogeneous Media. SPE-195310-PA (2003). https://doi.org/10.2118/87334-PA

Khoshkalam, Y., Khosravi, M., Rostami, B.: Visual investigation of viscous cross-flow during foam injection in a matrix-fracture system. Physics of Fluids (2019). https://doi.org/10.1063/1.5079482

Kovscek, A.R., Patzek, T.W., Radke, C.J.: A mechanistic population balance model for transient and steady-state foam flow in Boise sandstone. Chemical Engineering Science (1995). https://doi.org/10.1016/0009-2509(95)00199-F

Kovscek, A.R., Radke, C.J.: Fundamentals of Foam Transport in Porous Media. In: Foams: Fundamentals and Applications in the Petroleum Industry, vol. 242. Advances in Chemistry, vol. 242, pp. 115-163. American Chemical Society, (1994)

Kovscek, A.R., Tang, G.Q., Radke, C.J.: Verification of Roof snap off as a foam-generation mechanism in porous media at steady state. Colloids and Surfaces A: Physicochemical and Engineering Aspects (2007). https://doi.org/10.1016/j.colsurfa.2007.02.035

Lv, M., Liu, Z., Ji, C., Jia, L., Jiang, Y.: Investigation of Pore-Scale Behaviors of Foam Flow in a Polydimethylsiloxane Micromodel. Industrial & Engineering Chemistry Research (2018). https://doi.org/10.1021/acs.iecr.8b03366

Marchalot, J., Lambert, J., Cantat, I., Tabeling, P., Jullien, M.C.: 2D foam coarsening in a microfluidic system. EPL (Europhysics Letters) (2008). https://doi.org/10.1209/0295-5075/83/64006

Moffitt, P., Pecore, D., Trees, M., Salts, G.: East Vacuum Grayburg San Andres Unit, 30 Years of CO2 Flooding: Accomplishments, Challenges and Opportunities. Paper presented at the SPE Annual Technical Conference and Exhibition,

Pancharoen, M., Fernø, M., Kovscek, A.: Modeling foam displacement in fractures. Journal of Petroleum Science and Engineering (2012). https://doi.org/10.1016/j.petrol.2012.11.018

Radke, C.J., Gillis, J.V.: A Dual Gas Tracer Technique for Determining Trapped Gas Saturation During Steady Foam Flow in Porous Media. Paper presented at the SPE Annual Technical Conference and Exhibition, New Orleans, Louisiana, 1990/1/1/

Rangel-German, E.R., Kovscek, A.R.: A micromodel investigation of two-phase matrix-fracture transfer mechanisms. Water Resources Research (2006). https://doi.org/10.1029/2004wr003918

Ransohoff, T.C., Radke, C.J.: Mechanisms of Foam Generation in Glass-Bead Packs. SPE Reservoir Engineering (1988). https://doi.org/10.2118/15441-PA

Rognmo, A.U., Fredriksen, S.B., Alcorn, Z.P., Sharma, M., Føyen, T., Eide, Ø., Graue, A., Fernø, M.: Pore-to-Core EOR Upscaling for CO2 Foam for CCUS. SPE-195310-PA (2019). https://doi.org/10.2118/190869-PA

Rossen, W.R.: Foam Generation at Layer Boundaries in Porous Media. SPE-195310-PA (1999). https://doi.org/10.2118/59395-PA

Rossen, W.R.: A critical review of Roof snap-off as a mechanism of steady-state foam generation in homogeneous porous media. Colloids and Surfaces A: Physicochemical and Engineering Aspects (2003). https://doi.org/10.1016/S0927-7757(03)00309-1

Rossen, W.R., Gauglitz, P.A.: Percolation theory of creation and mobilization of foams in porous media. AIChE Journal (1990). https://doi.org/10.1002/aic.690360807

Rossen, W.R., Shi, J., Zeilinger, S.C.: Percolation modeling of foam generation in Porous media. AIChE Journal (1994). https://doi.org/10.1002/aic.690400618

Saint-Jalmes, A.: Physical chemistry in foam drainage and coarsening. Soft Matter (2006). https://doi.org/10.1039/B606780H

Shah, S.Y., Wolf, K.-H., Pilus, R.M., Rossen, W.R.: Foam Generation by Capillary Snap-Off in Flow Across a Sharp Permeability Transition. SPE-195310-PA (2019). https://doi.org/10.2118/190210-PA

Simjoo, M., Zitha, P.L.J.: Modeling and Experimental Validation of Rheological Transition During Foam Flow in Porous Media. Transport in Porous Media (2020). https://doi.org/10.1007/s11242-019-01251-9

Stephenson, D. J., Graham, A. G., & Luhning, R. W. (1993). Mobility Control Experience in the Joffre Viking Miscible CO2 Flood. SPE Reservoir Engineering, 8(03), 183-188. doi:10.2118/23598-pa

Stone, H.L.: Probability Model for Estimating Three-Phase Relative Permeability. SPE-2116-PA (1970). https://doi.org/10.2118/2116-PA

Szafranski, R., Lawson, J.B., Hirasaki, G.J., Miller, C.A., Akiya, N., King, S., Jackson, R.E., Meinardus, H., Londergan, J.: Surfactant/foam process for improved efficiency of aquifer remediation. In, Darmstadt 1998. Structure, Dynamics and Properties of Disperse Colloidal Systems, pp. 162-167. Steinkopff

Tang, G.-Q., Kovscek, A.: Trapped gas fraction during steady-state foam flow. Transport in porous media (2006). https://doi.org/10.1007/s11242-005-6093-4